

Correlative EBSD and SKPFM characterisation of microstructure development to assist determination of corrosion propensity in grade 2205 duplex stainless steel

C. Örnek¹  · D. L. Engelberg¹

Received: 28 June 2015 / Accepted: 12 October 2015 / Published online: 28 October 2015
© The Author(s) 2015. This article is published with open access at Springerlink.com

Abstract Correlative electron backscatter diffraction (EBSD) and scanning Kelvin probe force microscopy (SKPFM) analysis has been carried out to characterise microstructure development and associated corrosion behaviour of as-received and 750 °C heat-treated grade 2205 duplex stainless steel. High-resolution EBSD analysis revealed the presence of σ - and χ -phase, secondary austenite, Cr_2N , and CrN after ageing treatment. SKPFM Volta potential measurements confirmed the formation of discrete reactive sites, indicating local corrosion propensity in the microstructure. Cr_2N , σ -phase, and inter-granular χ -phase had the largest net cathodic activity, followed by CrN and intra-granular χ -phase showing medium electrochemical activity, with ferrite and austenite (including secondary austenite) showing net anodic activity. Corrosion screening confirmed selective corrosion of ferrite in the as-received and 750 °C-aged conditions with the corrosion propensity of secondary phases staying in-line with SKPFM observations. Stress corrosion micro-cracks were also observed and are discussed in light of microstructure corrosion propensity.

Introduction

Duplex stainless steels (DSS) offer a synergistic combination of excellent mechanical properties with enhanced corrosion resistance, and these materials are now increasingly used, such as the manufacture of containers for the storage of intermediate-level radioactive waste (ILW) [1]. Heat treatment, welding, or prolonged exposure to elevated temperatures may lead to undesired phase reactions in these high-alloyed stainless steels [2–5]. For example, the ferrite can decompose into a series of meta-stable and thermodynamically stable phases, whilst the austenite has often been stated to be unaffected [2, 4, 6]. However, phase reactions can also occur in the austenite, increasing the volume fraction of secondary phase products in the microstructure [7–13]. Components made with large wall thicknesses, therefore, usually contain intermetallic phases due to variations in cooling rates after high temperature treatments, with the core of components typically containing large volume fractions [14, 15].

Phase reactions are more favoured in the ferrite due to the enrichment of Cr and Mo, combined with far higher diffusion rates compared to the austenite [3, 4, 16]. For example, phase reactions in the temperature range between 250 and 550 °C have been known as ‘475 °C embrittlement’ [2–5, 17, 18] where in addition to the degradation of mechanical properties a significant reduction in corrosion performance has also been observed [17–21]. Phase reactions occurring in the temperature range between 600 and 1000 °C have become known as ‘ σ -phase embrittlement’ where numerous secondary phases, such as Frank–Kasper phases (σ and χ) and, to some extent, R-phase can be formed [5, 10, 16, 22–35]. These are often accompanied by the precipitation of nitrides (Cr_2N and CrN) and carbides [2, 4, 5, 16, 34, 36, 37].

✉ C. Örnek
cem.oernek@manchester.ac.uk

D. L. Engelberg
dirk.engelberg@manchester.ac.uk

¹ Materials Performance Centre & Corrosion and Protection Centre, School of Materials, The University of Manchester, Sackville Street Campus, Manchester M13 9PL, UK

Determination of the identity and the volume fraction of secondary phases have typically been carried out using image analysis of optical and/or electron microscopic micrographs, often supported by analytical semi-quantitative assessment of the chemical composition by energy-dispersive X-ray (EDX) analysis. However, uncertainty and lack of precision of these measurement methods did generally not allow to build-up a comprehensive mechanistic understanding of the behaviour of intermetallic phases during corrosion processes. Investigations to quantitatively describe microstructure development of aged duplex stainless steels at elevated temperatures, especially with respect to the formation of secondary phases, has often been associated with σ - and χ -phase formation based on eutectoid decomposition reaction of the ferrite. The effects of other precipitates such as Cr-nitrides were often not taken into account due to their small volume fractions and geometrical sizes, which makes them difficult to detect [3, 4, 16, 26, 34, 38].

The electron backscatter diffraction (EBSD) technique has developed into a tool for precise mapping of the microstructure for texture, crystallographic phases, and identification of misorientation gradients with information about local plastic strain. Mapping of multiple phases over large areas with high spatial resolution of up to 10's of nm has become possible for quantitative identification of crystallographic information to allow in- and ex situ observation of microstructure development [39]. EBSD combined with scanning Kelvin probe force microscopy (SKPFM) can provide crystallographic information about the microstructure with local Volta potential information at high spatial resolution (10's of nm's). The latter is a quantitative measure to describe electrochemical reactivity of a metal surface [40–44]. The knowledge about local Volta potential differences allows characterisation of corrosion processes, for example, to understand local micro-galvanic coupling which has importance in bi-phase alloys such as duplex stainless steels [13, 45–50]. Selective dissolution of the ferrite phase in duplex stainless steels, for example, can be explained by the larger Volta potential difference with respect to the Pt reference (lower absolute Volta potential), compared to a smaller measured difference of the austenite [18, 45, 46]. With the introduction of cold work, grade 2205 duplex stainless steel tends to show preferential local corrosion sites associated with localised deformation in the austenite, with these regions related to local Volta potential extremes [45, 51].

The purpose of the work reported in this paper was to link the precipitation of secondary phases after 750 °C heat treatment using multi-scale EBSD analysis, to their Volta potential differences using SKPFM. Information from correlative EBSD and SKPFM analysis provides an insight

into mechanistic understanding of the atmospheric corrosion and stress corrosion cracking (AISCC) behaviour of grade 2205 duplex stainless steel microstructure.

Experimental

A solution-annealed (as-received) grade 2205 duplex stainless steel plate of 10 mm thickness was used in this work with a composition shown in Table 1. EDX spectroscopy measurements of the ferrite and the austenite phases were conducted to inform about alloy partitioning, with the results also provided in Table 1. Small miniature tensile samples were manufactured with an overall length of 50 mm, a thickness of 1 mm, with 25 mm gauge length, and 3 mm gauge width, as well as coupon samples with dimensions of 10 mm \times 10 mm \times 10 mm (L \times W \times T). All samples were aged for 5 h at 750 °C, followed by air-cooling to room temperature. The surface of these samples was mechanically ground to 4000-grit using SiC paper, followed by a 3, 1, 1/4, and 0.1 μ m diamond paste polishing finish. A final fine-polishing treatment using a modified OP-S suspension (OP-S with a few drops of concentrated HNO₃ and H₂SO₄) was performed for one hour to achieve a smooth, strain-free surface finish for EBSD and SKPFM analysis.

Microstructure analysis

The microstructures of as-received and heat-treated specimens were analysed by EBSD using an FEI Magellan high-resolution scanning electron microscope (SEM). Data acquisition was performed with a Nordlys EBSD detector from Oxford Instruments with AZtec 2.2 software. An accelerating voltage of 10–20 kV was used with low current (spot size) to achieve effective spatial resolutions of 10's of nm [39, 52]. High-resolution EBSD mapping was carried out with step-sizes between 56 and 75 nm over an area of 100 μ m \times 87 μ m. For the identification of crystallographic phases, the parameters listed in Table 2 were used. The phase databases were included in AZtec software. Databases from HKL and Inorganic Crystal Structure Database (ICSD) were used for phase acquisition.

Indexing rates were typically close to 99 % and at least six Kikuchi bands were selected for successful phase identification, with the minimum number of detected bands of the corresponding Kikuchi diffraction pattern for each phase given in Fig. 1. Extra care was taken for indexing secondary phases, such as CrN, Cr₂N, and χ -phase. Data acquisition was first performed using all listed phases. When secondary precipitates were indexed, the dataset was re-assessed by de-selecting individual phases and re-mapping the same area without the corresponding phase. Phase

Table 1 Chemical compositions (wt%) of grade 2205 duplex stainless steel used in this study

Grade	C	Si	Mn	P	S	Cr	Ni	Mo	N	Fe
Plate	0.016	0.4	1.5	0.021	0.001	22.4	5.8	3.2	0.18	bal.
Ferrite	n.a.	0.5	1.7	n.a.	n.a.	25	4.3	4.3	n.a.	bal.
Austenite	n.a.	0.4	1.9	n.a.	n.a.	22.1	6.9	2.4	n.a.	bal.

Semi-quantitative EDX analysis of the ferrite and austenite composition is also provided to inform about element partitioning (n.a. = not analysed)

Table 2 Database with crystallographic geometry parameters for EBSD phase identification

Phase	<i>a</i> (Å)	<i>b</i> (Å)	<i>c</i> (Å)	α	β	γ	Space group	Database
Ferrite	2.87	2.87	2.87	90°	90°	90°	229	HKL
Austenite	3.66	3.66	3.66	90°	90°	90°	225	HKL
Cr ₂ N	4.75	4.75	4.43	90°	90°	120°	162	ICSD
CrN	2.97	4.12	2.88	90°	90°	90°	59	ICSD
Sigma	8.80	8.80	4.56	90°	90°	90°	136	HKL
Chi	8.92	8.92	8.92	90°	90°	90°	217	HKL
Cr ₂₃ C ₆	10.6	10.6	10.6	90°	90°	90°	62	ICSD

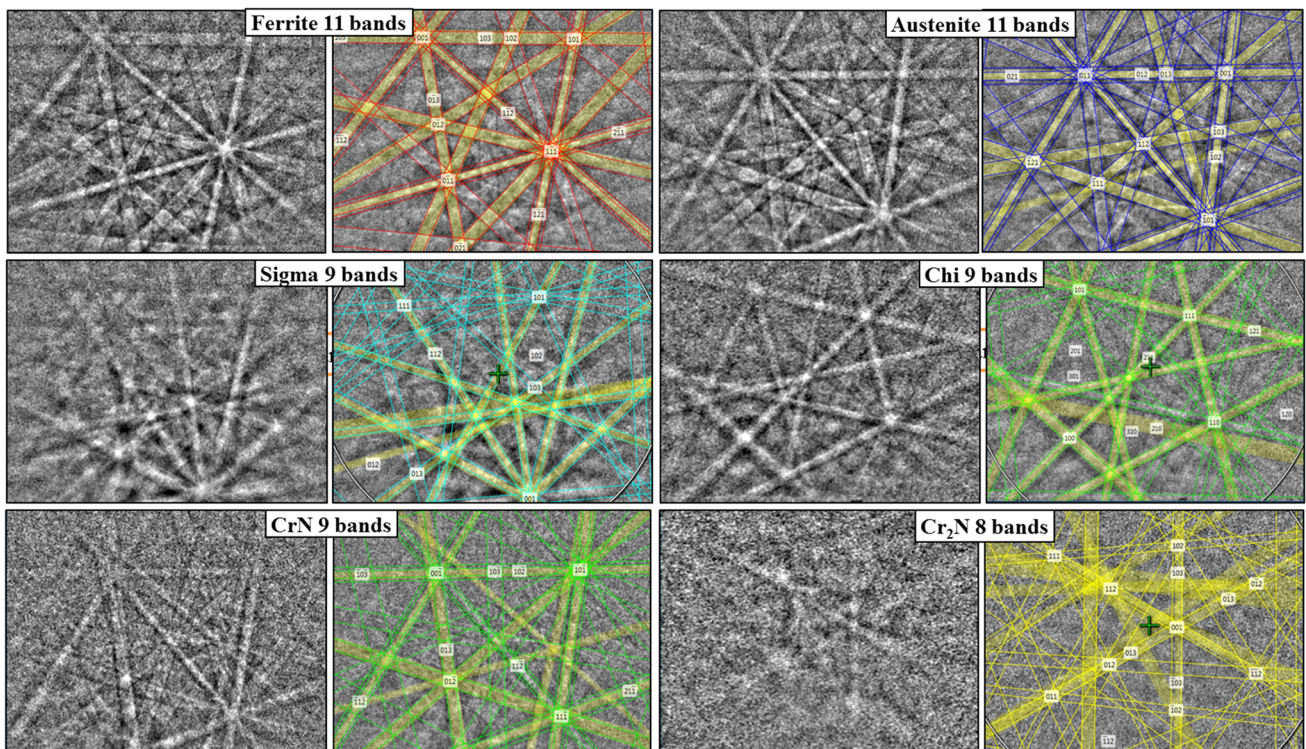


Fig. 1 Kikuchi diffraction bands of all indexed phases in our study. Each image pair shows unsolved (*left*) and solved (*right*) Kikuchi pattern with the minimum number of bands detected for each phase

identification proved to be reliable when the previously indexed region of a secondary phase was non-indexed, which confirms and validates the indexing procedure for CrN, Cr₂N, χ , and σ -phase. Indexing of chromium carbides (Cr₂₃C₆) for example, revealed to be problematic, since the ferrite or austenite were mis-indexed when the Cr₂₃C₆

phase was selected for acquisition. EBSD assessment of Cr₂₃C₆ was, therefore, excluded in our assessment. However, carbide formation in the 750 °C temperature range is extremely retarded in modern duplex stainless steel, with nitrides usually formed in far larger quantities leading to a suppression of carbide formation [16, 34].

All EBSD maps were processed using HKL Channel 5 software, and phase fractions and grain sizes were extracted. High-angle grain boundaries (HAGB's) were determined with misorientation in excess of 15° , and low-angle grain boundaries (LAGB's) were defined with 1° – 15° . Phase maps were generated with all phases detected, including phase and grain boundaries.

Scanning Kelvin probe force microscopy

SKPFM and Magnetic Force Microscopy (MFM) measurements were carried out with a *Dimension 3100* atomic force microscope (AFM) from *Veeco* interfaced with a *Nanoscope 3a* controller. Pt-coated *OSCM-PT* AFM probes from *Olympus* with 15 nm nominal radius were used to map the surface topography and the corresponding Volta potential difference of the metal with respect to the tip. The scan size of AFM map was between 10 and 80 μm , depending on the microstructural features to be characterised. The scan rate was adjusted to the tip velocity (10–30 $\mu\text{m/s}$), which corresponds to a scan rate of 0.2–0.5 Hz. The images contained 512×512 pixels yielding effective spatial resolution between 20 and 156 nm. All maps were processed using *Nanoscope VI.5* software (*Bruker*). Topography/height and potential maps were flattened with 0th flattening order to achieve best contrast within the microstructure; therefore, all data are semi-quantitative only.

In this paper, and for the probes used, higher potentials indicate a larger potential difference and correspond to anodic sites due to a larger absolute work function difference between the bias-controlled AFM tip and the microstructure feature of the grounded sample. According to this definition, cathodic sites have, therefore, lower Volta potentials than their anodic counter-parts [53]. More comprehensive explanation about the meaning of the potential and the Kelvin probe technique can be found elsewhere [43–45, 50, 54, 55].

Atmospheric-induced stress corrosion cracking testing (AISCC)

AISCC susceptibility was investigated on as-received and 750 °C heat-treated mini-tensile specimens, which were ground to 4000-grit using SiC sand papers. The heat-treated specimen, however, was afterwards electro-polished in an electrolyte of a mixture of 20 % perchloric acid and 80 % methanol at 20 V and at a temperature of -40°C . This was done to achieve smooth surface finish for phase identification after the corrosion test.

The as-received and heat-treated mini-tensile specimens were strained to 3 and 1 %, respectively, in self-designed direct tension rigs [56]. A strain gauge was placed on the

backside of each specimen and the sample extension monitored, in situ, using a LabVIEW programme. Water droplets containing MgCl_2 in different concentrations and volumes were applied onto the surface. The droplets were dispensed with an Eppendorf micropipette. Nominal deposition densities of magnesium chloride and chloride ions were calculated from area measurements as listed in Table 3. The deposited droplets changed their shape during exposure due to secondary spreading (see Fig. 2 for images after exposure); therefore, the determined 'initial' deposition densities most likely changed over time.

The direct tension rigs were placed in a climatically controlled KBF Binder cabinet for 259 days at 50 °C and 30 % relative humidity (RH); however, fluctuations in RH up to 60 % were observed during the last 2 weeks of exposure associated with equipment problems, therefore, the test was terminated. During the time of exposure, the direct tension rigs were periodically removed from the humidity chamber to assess whether corrosion had occurred. After terminating the test, the sample was rinsed in distilled water to dissolve salt and corrosion products, followed by an additional cleaning cycle in a 10 wt% citric acid solution at 80 °C for 2 h to remove remaining corrosion products.

Results and discussion

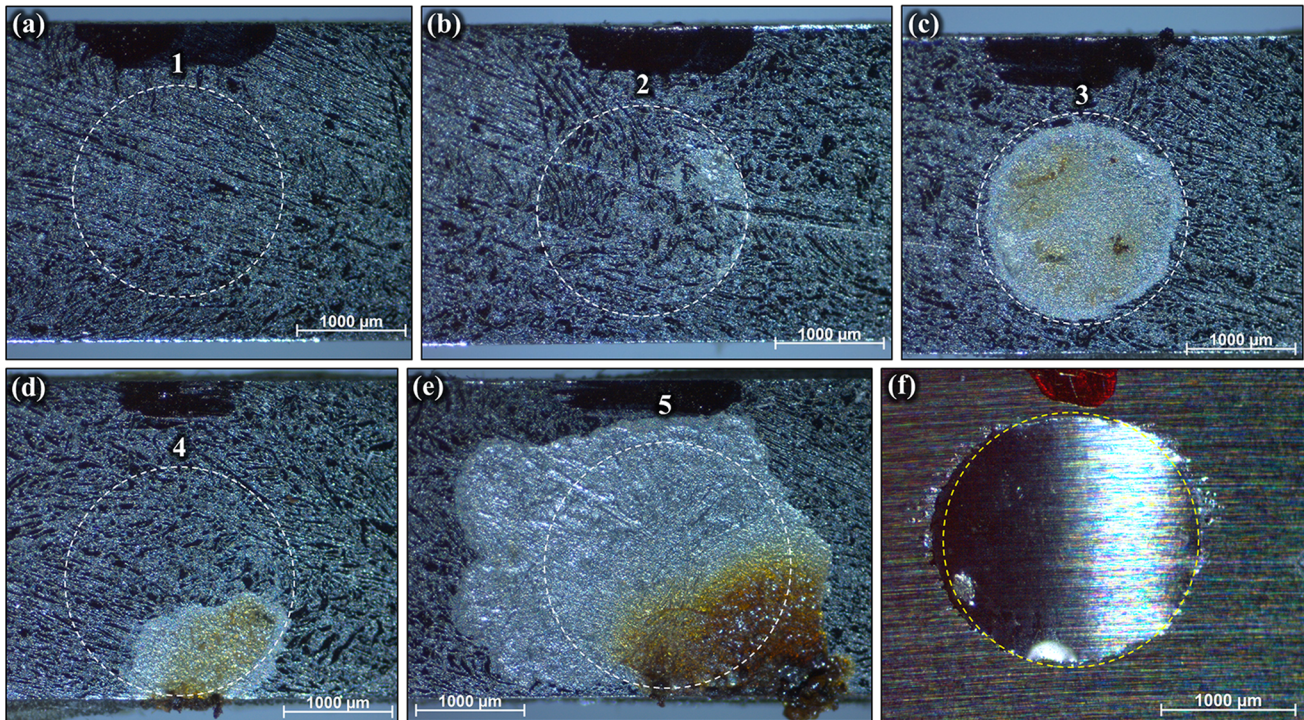
EBSD microstructure characterisation

The microstructure of the as-received and heat-treated condition is shown as EBSD phase maps in Fig. 3(a, b). The as-received microstructure consisted of $44 \pm 2\%$ ferrite (δ) and $56 \pm 2\%$ austenite (γ). The ferrite formed the matrix with the austenite present in the form of island-like discrete grains or clusters of small grains. The shape of ferrite and austenite grains was elongated due to the hot rolling process during manufacture. The austenite contained large fractions of twin boundaries, shown by the straight lines (yellow) in Fig. 3a, with interphase boundaries indicating more concave and convex shapes. The misorientation variation within ferrite and austenite grains was low. The average grain size of ferrite and austenite was 7 ± 1 and 6.5 ± 1 μm , respectively.

The specimen aged at 750 °C in Fig. 3b contained a large fraction of secondary phases, including σ -, χ -, chromium nitrides (Cr_2N , CrN), and secondary austenite (γ_2) which have formed during the ageing treatment [16, 30]. The normalised phase fraction results are shown in Table 4. High-resolution EBSD maps allowed clear observations of the newly formed microstructure shown in Fig. 4a–g. The austenite grain boundaries at the interphase had convoluted morphologies, with newly formed

Table 3 Experimental conditions of the AISCC test

Sample	Strain applied	No. of deposit	Volume (μl)	Droplet radius (mm)	Deposited MgCl_2 ($\mu\text{g}/\text{cm}^2$)	Deposited chloride ($\mu\text{g}/\text{cm}^2$)
As-received	3 %	1	0.5	1.78	1947	1450
Aged at 750 °C/5 h/air	1 %	1	0.5	1.78	20	14.5
		2	0.5	1.78	195	145
		3	0.5	1.78	1947	1450
		4	1.5	2.3	3319	2472
		5	2.5	2.8	3835	2856

**Fig. 2** Stereo-microscopy images of exposed electrolyte droplets containing magnesium chloride **a–e** of specimen aged at 750 °C (droplet 1–5) and **f** of as-received sample after exposure to 30 % relative humidity at 50 °C for 259 days

secondary austenite protruding from primary austenite islands as can be seen in Fig. 4a.

The ferrite is thermodynamically unstable and has decomposed [3, 4, 16, 34, 38], with three mechanisms proposed for secondary austenite formation where the eutectoid equilibrium $\delta \rightarrow \sigma + \gamma_2$ is the predominant reaction in the 700–900 °C temperature range. The overall fraction of secondary austenite formed was approximately 12 %, which was determined by the difference between pre- and post-ageing austenite contents. The eutectoid reaction mainly takes place at δ/γ -interphase boundaries due to increased diffusion rates, leading to segregation of Cr and Mo resulting in σ -phase formation [4, 12, 16, 26, 30, 32, 34]. The morphology of σ -phase often shows an allotriomorphic appearance due to its preferential growth

along phase boundaries and towards ferrite grain interiors [57]. The surrounding regions are then depleted in Cr and Mo, resulting in the formation to secondary austenite [4, 16, 57]. The eutectoid secondary austenite can have a similar appearance to that of σ -phase, as can be seen in Figs. 3b and 4a, b. Secondary austenite in direct contact with primary austenite can also form by growth towards ferrite regions and assume coagulant-like shapes with similar grain orientation as the primary austenite, also shown in Fig. 4e.

Austenite forming onto primary austenite has also been described as new austenite in the literature [58], but in our case all newly formed austenite induced by ageing is denoted as ‘secondary austenite’ (γ_2). Both types of secondary austenite have been found to contain reduced Cr

Fig. 3 EBSD phase maps showing **a** as-received microstructure and **b** microstructure after heat treatment at 750 °C for 5 h. Black lines are phase and high-angle grain boundaries. Note that Cr₂N and CrN are not visible at this scale (Color figure online)

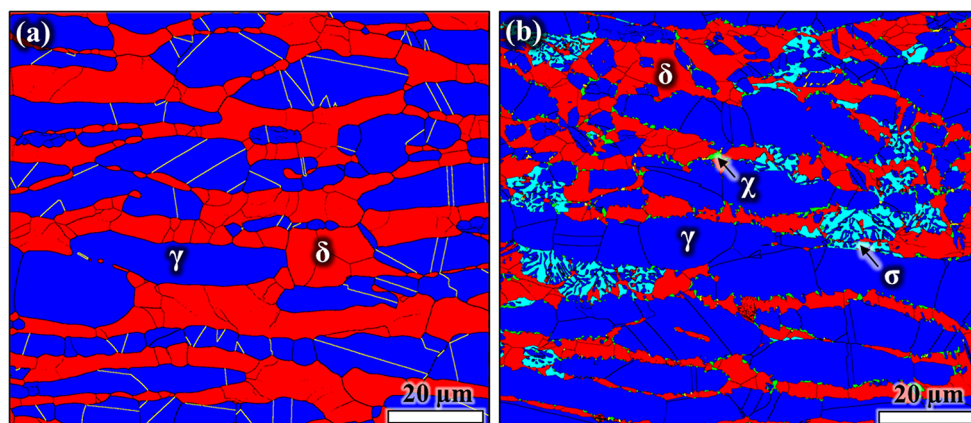


Table 4 Normalised EBSD phase fractions

Condition	δ	γ	σ	χ	CrN	Cr ₂ N
As-received	44	56	n/a	n/a	n/a	n/a
Aged 750 °C/5 h	26	65.5 ^a	5.6	2.1	0.4	0.33

n/a not available

^a Secondary austenite included

contents, particularly if the formation of Cr-rich precipitates is involved, such as σ -phase [30, 59]. The volumetric fraction of secondary austenite is typically twice that of formed σ -phase, clearly indicating faster reaction kinetics [30]. The corrosion performance of microstructures containing secondary austenite has been reported to cause reduced pitting corrosion resistance [37, 60]. Therefore, the fraction of σ -phase alone is an insufficient parameter for microstructure assessment regarding the corrosion behaviour of duplex stainless steels.

The newly formed secondary austenite had similar grain orientation to the existing austenitic phase, with neither new high-angle or low-angle grain boundaries seen in most newly formed austenite grains. The secondary austenite seemed to have developed through grain growth from primary austenite grains, indicated by the white dashed line in Fig. 4a, showing the approximate position of the initial δ/γ phase boundary. Secondary austenite formation was also observed through new austenite formation within ferrite regions associated with eutectoid σ -phase formation in the ferrite producing elongated lamellae-like shapes (allotriomorphic) also shown in Fig. 4a, b.

The decomposition of ferrite was accompanied by the formation of σ - and χ -phase. The σ -phase contained no high- and low-angle grain boundaries and showed allotriomorphic morphology. The σ -phase was located between pre-existing primary austenite islands, clearly evidencing that this phase formed by consuming ferrite. Ferrite–austenite phase boundaries and triple junctions of grain

boundaries have been reported to act as nucleation sites for σ -phase [16, 22–24, 26–28, 30, 32]. The formation of σ -phase occurred at discrete regions in the microstructure, resulting in clusters of σ -phase and secondary austenite as can be seen in Fig. 3b. Furthermore, σ -phase was also found in ferrite grains, highlighted in Fig. 4c. The measured fraction of σ -phase was almost 6 % (Table 4), which is in good agreement with the work of Michalska et al. who obtained 6–7 % σ -phase in grade 2205 after ageing at 750 °C for 5 h via conventional image analysis [26]. Elmer et al. also investigated σ -phase formation in grade 2205, and ageing at 750 °C for 10 h produced 22.7 % of σ -phase determined via in situ synchrotron X-ray diffraction technique [24]. They reported 90 % completion of phase reactions after 10 h ageing, and predicted an overall fraction of 24 % of σ -phase by ThermoCalc calculations [24]. The size of σ -phase was estimated in Fig. 4 using horizontal and vertical ferret diameters of 1–7 μm . However, the three-dimensional appearance may result in different ‘structural’ sizes due to the allotriomorphic shape of σ .

A total fraction of 2.1 % χ -phase was measured after ageing at 750 °C for 5 h in the microstructure, shown in Fig. 4. The χ -phase precipitated primarily at δ/γ phase boundaries, with expansion along the circumference of primary austenite grains but growth towards the ferrite. In addition, χ also consumed some austenite as can be seen in Fig. 4a–g. However, χ -phase precipitation is not restricted to ferrite or δ/γ phase boundary regions. In austenitic stainless steels, χ , σ , and other secondary phases can also form by consumption of austenite grains [10]. Therefore, similar reactions are also expected to occur in duplex stainless steels. The formation of χ -phase in grade 2205 duplex stainless steel has been reported to occur at temperature approximately 75 Kelvin below that of σ -phase formation, with fastest transformation kinetics at 750 °C [16, 30]. Therefore, χ -phase formation has been reported to be more favoured at the initial stages of ageing [16, 22, 26, 27, 30]. Padilha et al., for example, observed qualitatively

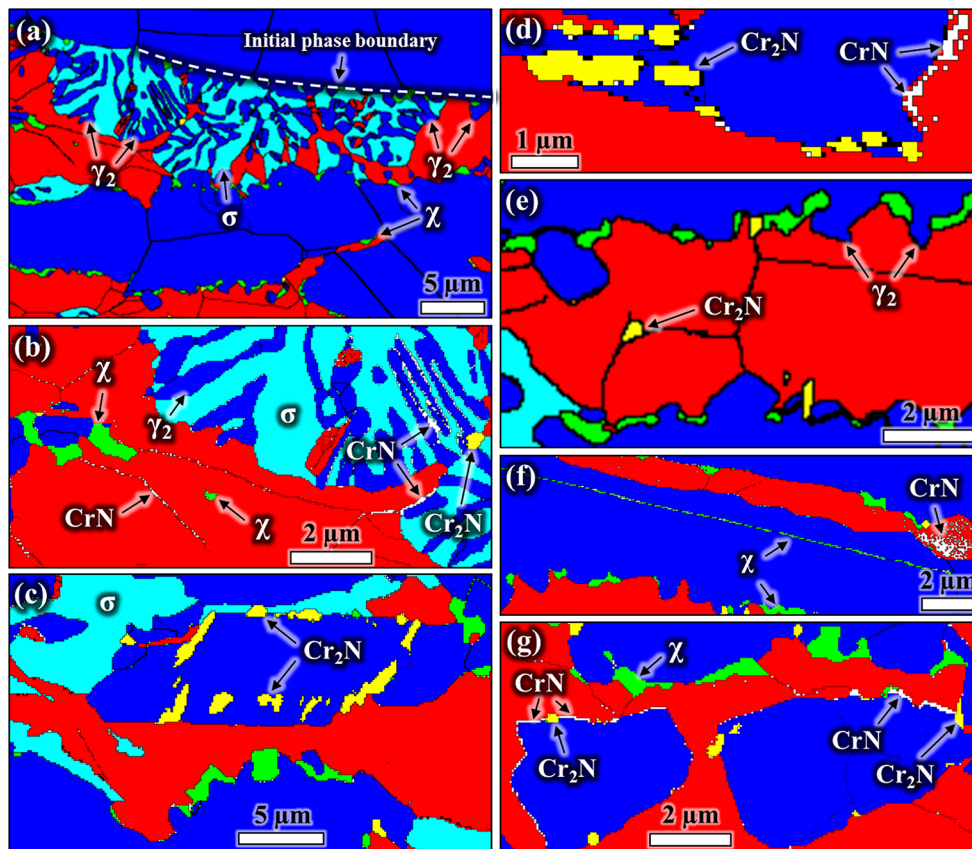


Fig. 4 High-resolution EBSD phase maps of the specimen aged at 750 °C for 5 h showing **a** σ , χ , and γ_2 formation, **b** intra-granular χ phase formation in ferrite with inter-granular CrN formation in ferrite and at σ/γ_2 interphase boundaries, **c**, **d** Cr_2N formation in austenite and at existing δ/γ phase boundaries, with **d** CrN formation at δ/γ

phase boundaries, **e** inter- and intra-granular Cr_2N formation in ferrite, **f** intra-granular CrN formation in δ and χ formation at boundaries and interphases, and **g** CrN, χ , and Cr_2N formation at interphase boundaries

larger fractions of χ than σ -phase at early ageing stages, with the χ -phase consumed by σ -phase formation after prolonged ageing treatment at 750 °C [30]. Several works have reported χ -phase as meta-stable [22, 30], although computational isothermal sections of Fe–Cr–Ni–Mo–N systems containing 22 % Cr and 5 % Ni predicted χ as a stable phase, co-existing with σ -phase and Cr_2N [16].

The size of χ -phase was estimated in Fig. 4 using horizontal and vertical ferret diameters of 0.1–2 μm . Transformation of χ occurred at multiple sites, resulting in a more homogenous formation in the microstructure compared to the clustered σ -phase appearance. The χ -phase precipitates also seemed to pin interphase boundaries, causing bulging of the newly formed secondary austenite, as shown in Fig. 4e. Moreover, it was noticed that χ -phase even nucleated within austenite grains, decorating part of a twin boundary, as shown in Fig. 4f.

Chromium nitrides, both CrN and Cr_2N , were observed after ageing at 750 °C. Both compounds can be seen in Fig. 4, with the orthorhombic CrN and the hexagonal Cr_2N decorating δ/γ , δ/γ_2 , and also σ/γ_2 interphase regions. The

Cr_2N had more discrete dimensions in the form of larger areas than CrN (Fig. 4). The morphology of Cr_2N was elongated and ellipsoid shaped. Their sizes varied between 130 nm to 4 μm with high aspect ratios. The CrN had smaller dimensions, typically between 80 and 620 nm, but CrN was often found in clusters as highlighted in Fig. 4f. The total fraction of Cr_2N was 0.33 % and the fraction of CrN was 0.41 %. There has been work published on Cr_2N and most is in agreement that Cr_2N is stable and co-exists with χ -phase and σ -phase precipitates [6, 10, 12–16, 27, 28, 34, 36, 48, 61, 62], but far less is known about CrN [11, 36].

The formation of Cr-nitrides is usually associated with increased ferrite contents in duplex stainless steels [11, 36, 61, 62], and large fractions of nitrides have, therefore, been observed in welds and heat-affected zones [11, 34]. The formation of Cr_2N has been reported to either occur during cooling, when ferrite is supersaturated with nitrogen leading to the formation of elongated and discretely-shaped intra-granular precipitates with $\langle 0001 \rangle_{\text{Cr}_2\text{N}} \parallel \langle 011 \rangle_{\delta}$ orientation relationship, or during isothermal ageing in the 700–900 °C temperature range where inter-granular Cr_2N

precipitates are formed on $\delta\delta$ - and $\delta\gamma$ -boundaries [16]. In our study, Cr_2N was observed not only at interphase boundaries, but also within austenite grains indicating that nitride precipitation may be possible in austenite as well, which can be clearly seen in Fig. 4c, d.

CrN formation occurred within the ferrite, mostly on δ/δ and δ/γ grain boundaries as shown in Fig. 4b–g. No CrN was observed in the austenite, but only on γ_2/σ phase boundary regions as shown in Fig. 4b. An orientation relationship between CrN and ferrite $\langle 110 \rangle_{\text{CrN}} \parallel \langle 111 \rangle_{\delta}$ and $\langle 001 \rangle_{\text{CrN}} \parallel \langle 1\bar{1}0 \rangle_{\delta}$ has been reported [11]. In a grade 2505 duplex stainless steel with 0.14 % N both types of Cr-nitrides were observed, when the microstructure was cooled with rapid cooling in the range of 40–150 K/s [11]. The reported CrN precipitates showed a film- or platelet-like appearance, with Cr_2N having a rod-like shape, with the latter forming in larger sizes than CrN precipitates [56].

Both Cr-nitrides are typically enriched in Cr, N, Fe, and Mo, but Cr_2N contains more Cr than CrN, whilst the opposite holds true for the N content [36, 62]. The extent of elemental depletion zones around these precipitates usually develops as a function of element enrichment within the precipitate and the volumetric size. Since Cr_2N is more enriched in Cr and has a larger size than CrN, it is, therefore, expected that Cr_2N yields larger Cr-depleted regions, resulting in an increased electrochemical activity associated with reduced corrosion resistance [13, 36, 47, 48, 61]. This assumption will be discussed in more detail in light of the SKPFM results.

SKPFM: Volta potential measurements

Maps showing the Volta potential differences measured over regions containing ferrite and austenite in the as-received microstructure with corresponding topography and magnetic frequency maps are shown in Fig. 5a–c. Regions showing low Volta potential differences were determined to be non-ferromagnetic and hence austenitic as can be seen in the magnetic frequency map in Fig. 5c, indicating net cathodic character. Vice versa, regions of high potential with net anodic character are ferritic, showing a magnetic frequency response. The Volta potential reflects the electronic activity of a metal, and the larger the potential difference with respect to Pt the lower the actual electronic activity leading to facilitated charge transfer during electrochemical reactions [40, 41]. However, this describes thermo-dynamic equilibrium conditions, and kinetic information cannot be extracted.

The ferrite showed 50–70 mV in average larger Volta potential values than the austenite indicating higher electrochemical activity. The Volta potential difference also indicated possible micro-galvanic activity between

austenite and ferrite, at which the latter was expected to form the net anode whilst austenite the net cathode. The potential variation across ferrite and austenite interphases was smooth with only minor potential gradients. A smooth potential gradient is indicative for non-heterogeneous activity, such as selective attack. Earlier work on grade 2205 duplex stainless steel clearly demonstrated the susceptibility of ferrite when exposed to chloride-containing environment, with the introduction of plastic deformation leading to local Volta potential extremes (hot spots) [63].

A Volta potential differences map with topography to screen the 750 °C-aged microstructure is given in Fig. 6a, b. The corresponding SEM image with EBSD phase map of the same region is given in Fig. 6c, d. Volta potential differences over ferrite and austenite in certain regions were nearly similar, which means that the driving force for galvanic coupling between those regions is reduced. However, local Volta potential extremes were developed indicating enhanced electronic activity and galvanic coupling between net anodic and net cathodic regions. The Volta potential variations within ferrite and austenite regions increased, indicating higher micro-galvanic activity within each phase. At this magnification, potential differences over secondary phases could not be discerned, and the mapped area in Fig. 6 was, therefore, re-scanned with higher resolution as shown in Figs. 7 and 8.

Figure 7 gives the Volta potential with corresponding EBSD map of an area containing intermetallic phases, showing numerous discrete regions with low and high potential variations and gradients. The line profile 1 in Fig. 7a, b, e shows that Cr_2N precipitates have the lowest Volta potential followed by austenite regions, with the latter possibly secondary austenite. This indicates low electronic activity of these phases. However, large potential gradients were found surrounding Cr_2N precipitates which gives an indication of local micro-galvanic cells with enhanced electronic coupling activity. Such large gradients adjacent to second phase precipitates are indicative of element depletion zones; hence, the adjacent regions often form local anodes. Cr_2N has been reported to contain higher Cr concentrations than CrN and χ , most likely resulting in concentration gradients during thermal treatments [11, 36]. Volta potential gradients measured adjacent to CrN and χ precipitates were far lower than those measured adjacent to Cr_2N . Sathirachinda et al. investigated the effect of thermally treated microstructure of grades 2205 and 2507 duplex stainless steel with SKPFM [13], measuring potential difference of 10–15 mV between γ and Cr_2N with respect to a Pt–Ir tip. The study concluded that Cr_2N has the highest practical nobility in the microstructure, which would mean net cathodic behaviour, in-line with our observations.

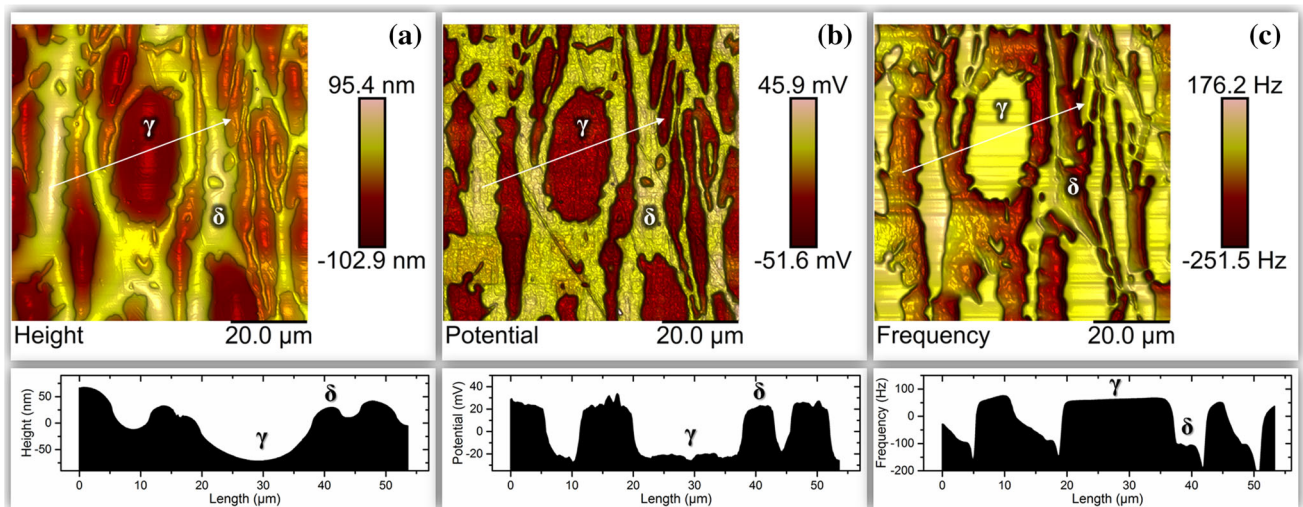
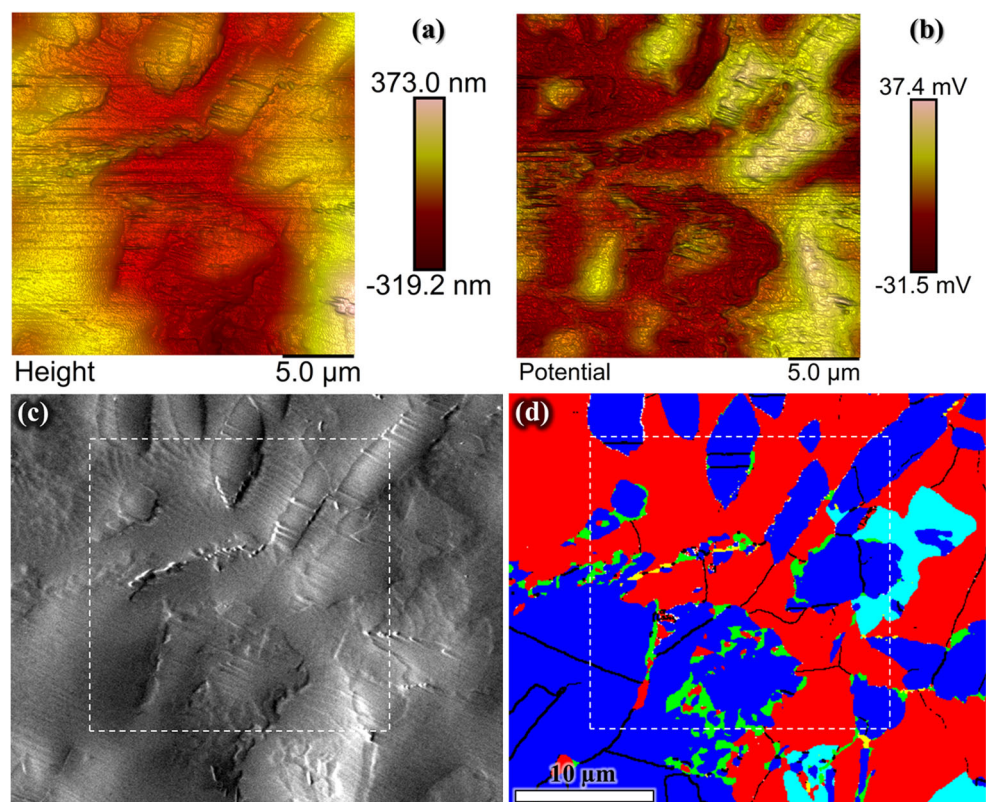


Fig. 5 SKPFM analysis of as-received microstructure with **a** topography of a scanned area of $80 \times 80 \mu\text{m}^2$ containing ferrite and austenite with a line profile measurement along the *white arrow* given

below, **b** the corresponding Volta potential differences map with a line profile, and **c** correlated magnetic frequency measured over the same area (note a small off-set of the scanned area) (Color figure online)

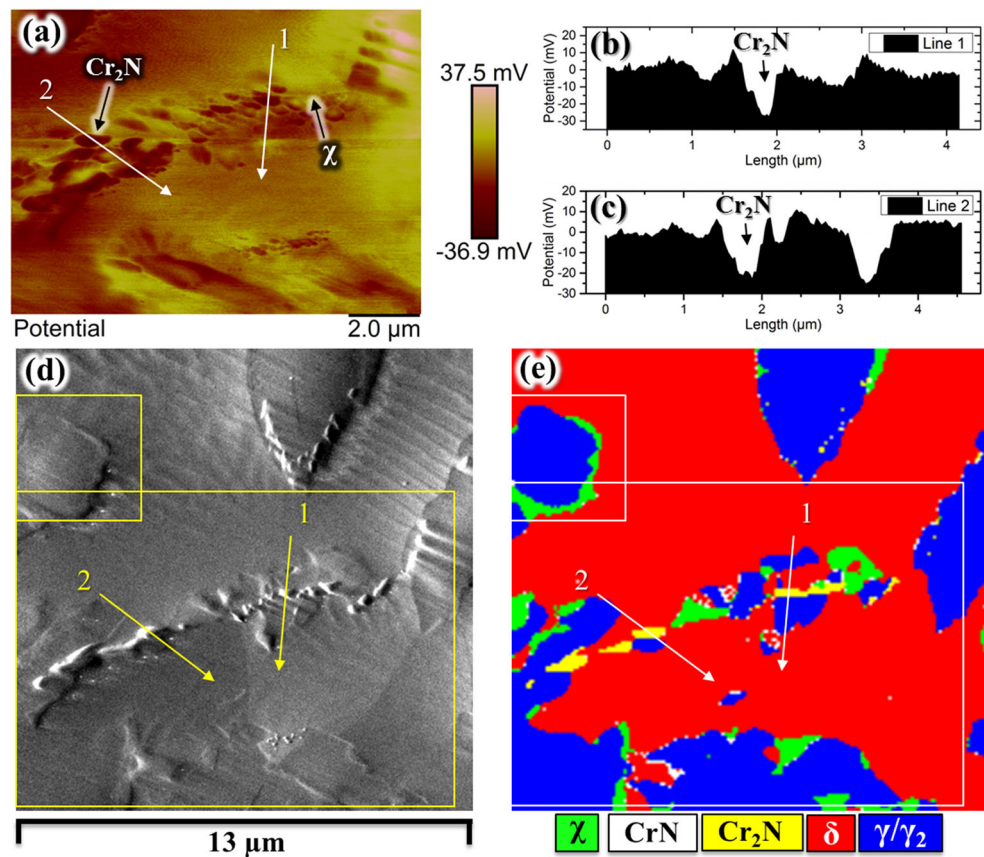
Fig. 6 SKPFM analysis of aged microstructure with **a** topography map, **b** corresponding Volta potential map, **c** corresponding SEM micrograph in secondary electron imaging mode, and **d** corresponding EBSD phase map showing γ/γ_2 (blue), δ (red), χ -phase (green), σ -phase (aqua), Cr_2N (yellow), CrN (white), and grain/phase boundaries (black). *Highlighted region* in **c**, **d** indicate the scanned area (Color figure online)



The χ -phase showed variations of its electronic behaviour over different areas, with some regions indicating net cathodic activity, whereas others showed net anodic character as can be seen in Fig. 7a, e. The χ -phase at δ/γ boundaries was denoted as ‘interphase/inter-granular- χ ’ (IP- χ) and the χ -phase within ferrite

labelled as ‘in-ferrite/intragranular- χ ’ (IF- χ). The IP- χ had more net cathodic character, whilst IF- χ seemed to be net anodic, suggesting that they have different chemical compositions, with the IP- χ phase probably more enriched in Cr and Mo. However, the potential gradients adjacent to IP- χ were far steeper than those

Fig. 7 Medium-resolution SKPFM analysis of aged microstructure: **a** Volta potential map, **b, c** measured line profiles (1, 2) in **a**, **d** corresponding SEM image, and **e** corresponding EBSD phase map. The large highlighted area in **e** shows the SKPFM measured region in **a** (Color figure online)



observed surrounding IF- χ , indicating the presence of depletion effects.

High-resolution Volta potential mapping was, therefore, performed on a region containing γ/γ_2 , χ -phase, and CrN (Fig. 8). Small finger-like globular features were apparent which were indexed by EBSD as CrN precipitates and shown in Fig. 8e, f. The CrN particles were next to χ -phase precipitates, embedded in the ferrite. Line profile measurements across the CrN precipitates showed a potential difference of 5–10 mV higher than the surrounding ferrite phase, with the depleted areas around these precipitates indicating 5–6 mV lower potentials than the ferrite. This clearly indicated that depleted regions would behave net anodic, whilst the CrN would behave net cathodic with respect to the ferrite phase. The IP- χ in Fig. 8 had 30–40 mV larger Volta potentials than the IF- χ shown in Fig. 7 despite their comparable dimensions. This potential difference supported different chemical compositions of this phase. Seemingly, the cathodic character was not only limited to the χ -phase.

The potential differences measured over all crystallographic phases are shown in Fig. 9. The Cr₂N phase showed the largest net cathodic behaviour, together with σ and IP- χ . The intra-granular IF- χ phase showed net anodic properties whilst the IP- χ phase was more cathodic.

Therefore, both χ -phase compositions are expected to behave differently. The nobility of CrN seemed to lie in-between the matrix phases and most other secondary phases. Volta potential values of ferrite and austenite had large scatters, with ferrite showing slightly more net anodic character than austenite. The scatter is partly due to large micro-galvanic activities observed within both matrix phases.

Stress corrosion screening tests

As-received microstructure

The as-received mini-tensile specimen dosed with 1450 $\mu\text{g}/\text{cm}^2$ MgCl₂ was exposed to 50 °C and 30 % RH, and after removing and cleaning the sample substantial corrosion attack was observed, which can be seen in Fig. 10a. Primarily the ferrite was corroded under the droplet deposit with some minor corrosion observed on the austenite. The same corrosion pattern has previously been reported under similar exposure conditions [45, 63, 64], with ferrite clearly the electrochemically more active phase leading to selective dissolution [17, 18, 44, 45, 56, 64–72]. The ferrite phase is, usually, the electrochemically more active phase in 2205 duplex stainless steel

Fig. 8 High-resolution SKPFM analysis of an area containing interphase χ (IP- χ) and CrN: **a** Volta potential map, **b–d** measured line profiles (1, 2, 3 in **a**), **e** 3D height map overlaid with Volta potential data, and **f** corresponding EBSD map (Color figure online)

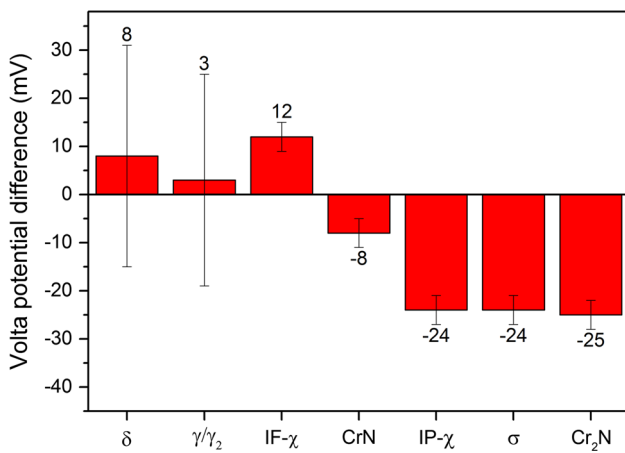
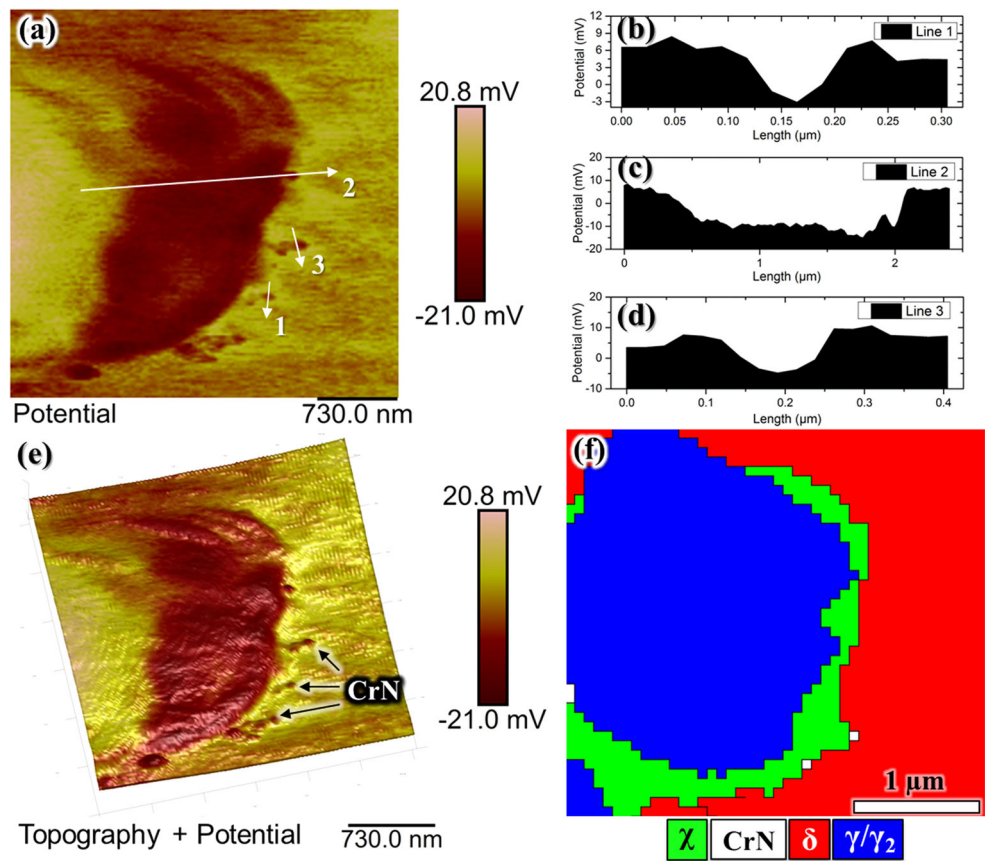


Fig. 9 Comparison of relative Volta potential differences of all observed phases after ageing in descending order from *left* (ferrite) to *right* (Cr₂N)

due to its lower corrosion potential in contrast to the austenite in mild chloride-bearing environments leading to micro-galvanic coupling between ferrite and austenite [66, 70, 73]. Selective corrosion of the ferrite, therefore, is often manifested as the main corrosion mechanism whilst the austenite is galvanically protected [17, 63, 72, 74–77].

High-resolution SEM assessment confirmed the presence of localised attack in the form of superficial sub-micrometre sized intra-granular corrosion pits on the austenite, with typical images shown in Fig. 10b, e. The attack on the austenite seemed to be related to slip bands and strain. The evolution of strain localisation in correlation with the development of local Volta potential extremes in austenite leading to enhanced propensity to localised corrosion with the introduction of cold deformation was earlier demonstrated [45]. Pitting corrosion on the austenite tended to suppress the selective dissolution of the ferrite. Seemingly, heterogeneous nucleation of numerous discrete corrosion pits on the austenite indicated those sites as more susceptible, possibly associated with strain localisation.

Some stress corrosion micro-cracks were also found in the austenite, oriented perpendicular to the applied stress direction (stress acted horizontal in Fig. 10c, e, f). The longest crack observed was less than 15 μm in length. Nucleation sites of cracks within existing cracks were also found, suggesting that some cracks may have stifled and stopped growing, before conditions for re-nucleating inside existing cracks were satisfied again. This is different from the classic stress corrosion cracking theory where cracks propagate with discrete steps. Figure 10e shows features related to crack nucleation inside an existing crack.

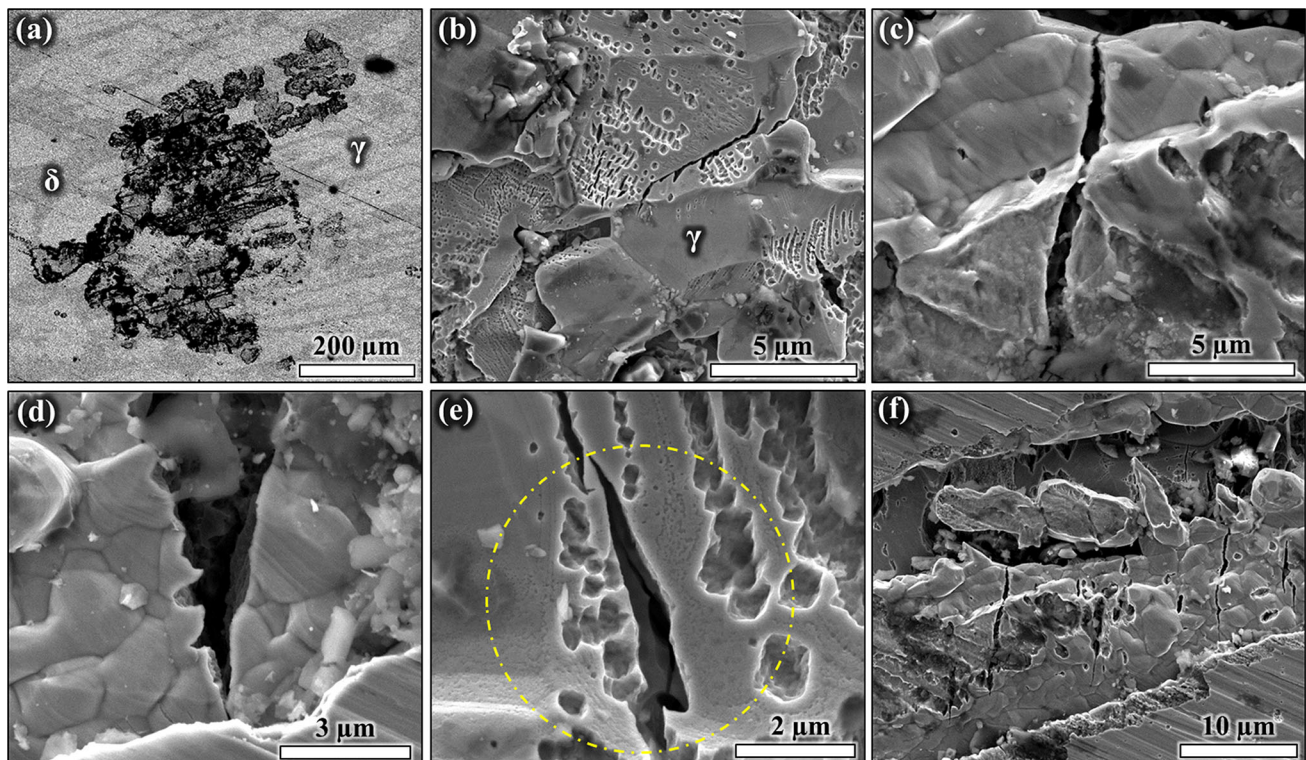
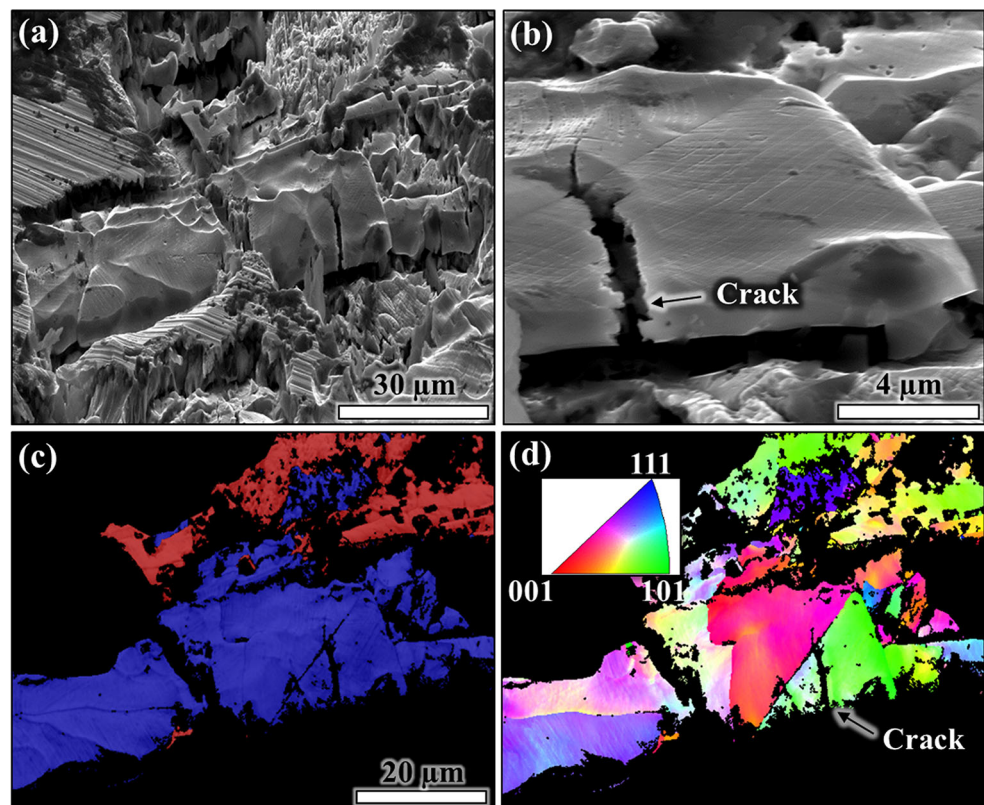


Fig. 10 Corrosion morphology of as-received microstructure after exposure to $1450 \mu\text{g}/\text{cm}^2$ MgCl_2 showing **a** the entire corroded area, **b** localised intra-granular corrosion attack on austenite, **c**, **d** stress corrosion micro-cracks on austenite, **e** multiple corrosion sites on

austenite with a crack inside a crack (within the *highlighted area*), **f** selectively dissolved ferrite regions with multiple cracks on austenite. The stress acted along the *horizontal direction*

Fig. 11 Corrosion morphology of as-received microstructure: **a** selective corrosion of ferrite (partially dissolved only) and **b** selective stress corrosion cracking of austenite with **c** corresponding EBSD phase map overlapped with band contrast map (austenite is *blue* and ferrite is *red* coloured), and **d** corresponding inverse pole figure map in *x* direction. Step size = 135 nm (Color figure online)



Retardation effects may have played an important part in crack development, for example, when the crack encounters γ/γ grain boundaries or δ/γ interphase boundaries. The stress corrosion micro-cracks observed were all transgranular in nature, and located in the austenite phase, as concluded from EBSD analysis seen in Fig. 11. Slip planes are easily noticed from SEM images, which play an active role in crack nucleation and growth. The crack in Fig. 11 initiated on a grain with close 101 orientation and grew towards

the grain interior before changing its direction slightly after encountering a boundary. A difference in crack opening is also observed with the crack wide open on one side of the grain boundary, and more tightly closed on the other.

Heat-treated microstructure

Figure 12a shows the specimen aged at 750 °C and exposed to 14.5 $\mu\text{g}/\text{cm}^2$ chloride for 259 days. Minor

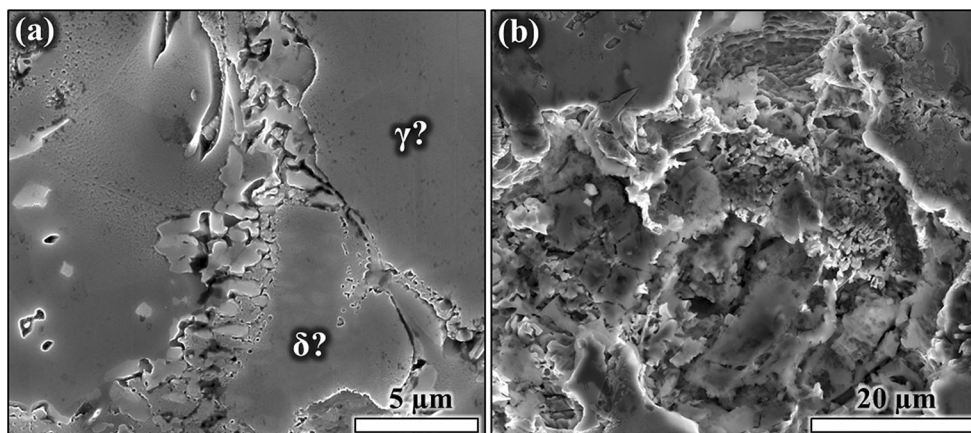


Fig. 12 Corrosion morphology of the aged specimen with 1 % elastic–plastic strain after 259 days exposure at 50 °C and 30 % RH: **a** minor corrosion attack under drop 1 (14.5 $\mu\text{g}/\text{cm}^2$) and **b** corrosion area under drop 3 (1450 $\mu\text{g}/\text{cm}^2$)

Fig. 13 Corrosion morphology of the aged sample under drop 2 (145 $\mu\text{g}/\text{cm}^2$) with **a** a corroded area, **b** higher-resolution image of the *highlighted box* in **a**, **c** selective dissolution of the ferrite with remainders of secondary phases, and cracked σ , and **d** fracture in σ phase

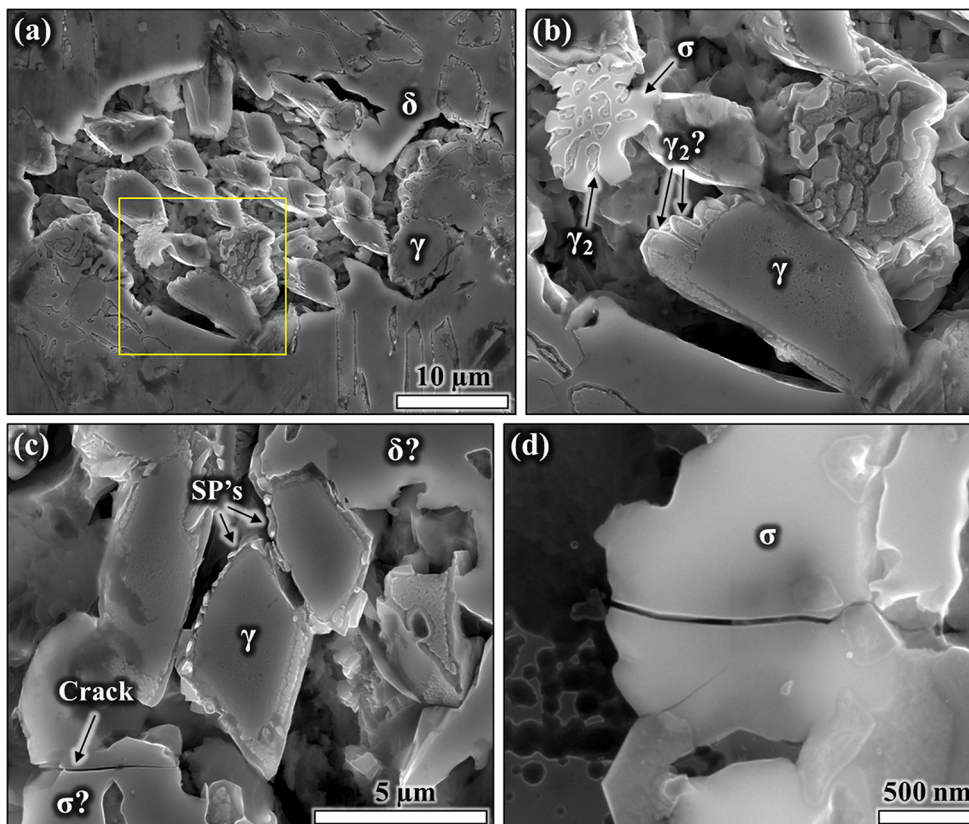
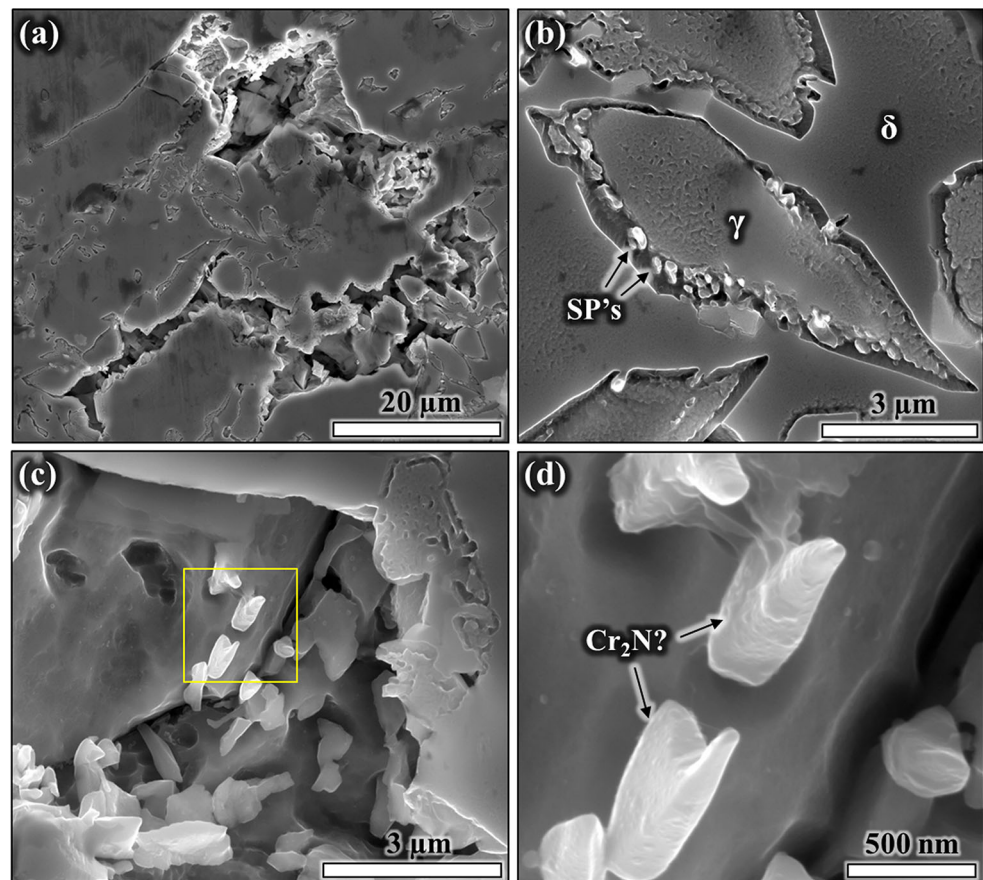


Fig. 14 Corrosion morphology of the aged sample under drop 4 ($2472 \mu\text{g}/\text{cm}^2$) with **a** selective corrosion of the ferrite, **b** selective attack along interphases with remaining secondary phases, **c, d** corrosion along interphase boundary regions with remaining secondary phases (possibly Cr_2N)



corrosion attack was only observed located at interphases and on the austenite, with some attack around secondary phases. Increasing the chloride concentration resulted in more severe attack as can be seen with a deposition density of $1450 \mu\text{g}/\text{cm}^2$ chloride (drop 3) in Fig. 12b. The attacked area and corroded volume of the 750°C -aged sample was significantly larger than that observed on the as-received specimen exposed with equivalent deposition density of chloride in Fig. 10a. However, no evidence for stress corrosion micro-cracking was found in these specimens. Stress corrosion cracking can only occur when the corrosion rate and crack velocity in that corrosion system have similar order of magnitude, but when corrosion reactions advance too fast, then crack nucleation and propagation are hindered.

The corrosion morphology of the aged sample after exposure to $145 \mu\text{g}/\text{cm}^2$ chloride (drop 2) indicated selective corrosion of the ferrite. However, high-resolution SEM analysis showed that selective corrosion of ferrite with some attack on the austenite occurred, shown in Fig. 13a, b. The σ -phase often remained in corroded regions, clearly indicating its net cathodic character, whereas ferrite and austenite were attacked, indicating their more net anodic character. In Fig. 13b, however, secondary

austenite remained unaffected after the corrosion test, indicated by the characteristic shape. A large number of smaller discrete precipitates can also be seen and these observations are in good agreement with the earlier Volta potential assessments, where such precipitates were measured to be net cathodic (Fig. 9). Thus, these precipitates are assumed to be Cr_2N , χ , and possible CrN on basis of their Volta potential response and morphological appearance.

A large σ -phase precipitated with a transgranular crack was also found, shown in Fig. 13c, d. A number of smaller cracks were also found, all located in the σ -phase indicating its brittleness and susceptibility to cracking. The presence of these cracks indicates an increased microstructure crack nucleation propensity, which was clearly enhanced by the presence of the brittle σ -phase in the microstructure.

The corrosion morphology under a chloride deposition density of $2472 \mu\text{g}/\text{cm}^2$ (drop 4) is shown in Fig. 14a. Selectively corroded ferrite regions can clearly be seen indicating the net anodic character during the corrosion process. Several corroded regions located along δ/γ interphases are also shown in Fig. 14b, decorated with secondary phases (SP) that seemed almost unaffected by the

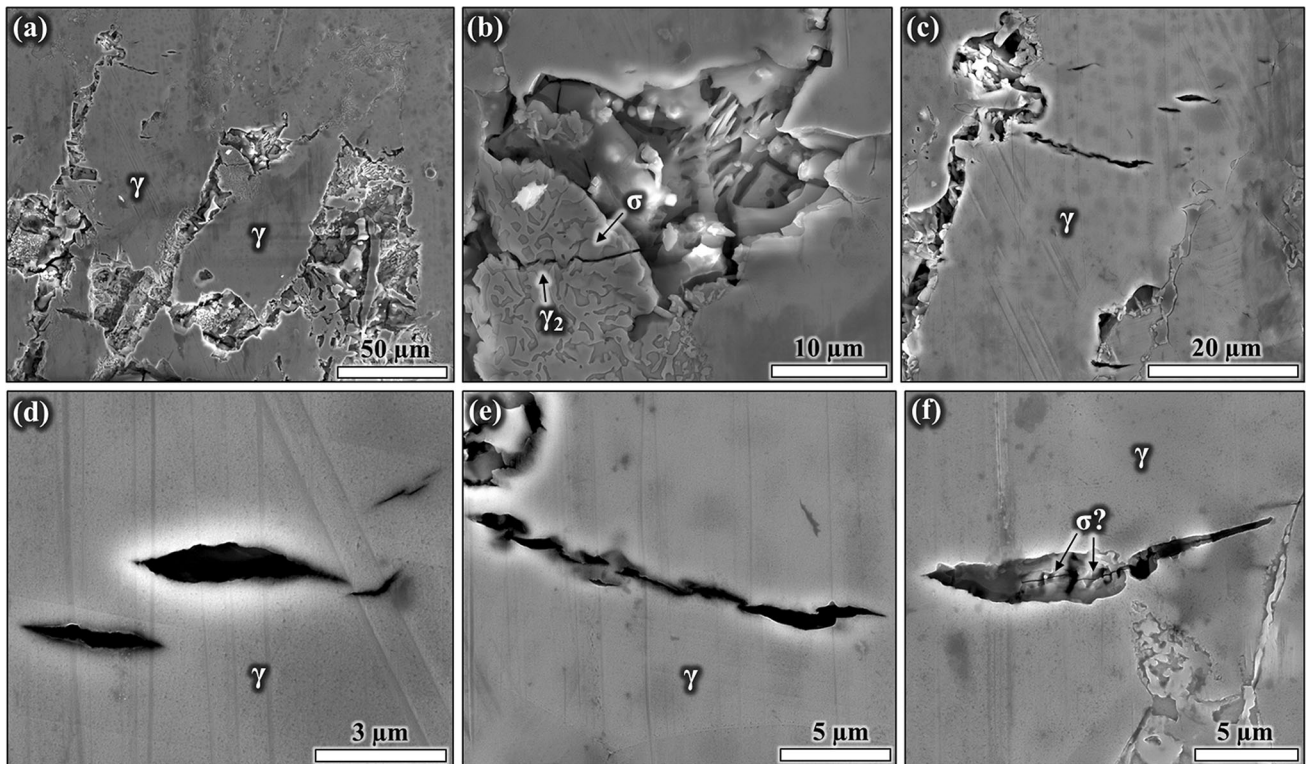


Fig. 15 Corrosion morphology of the aged sample under drop 5 ($2856 \mu\text{g}/\text{cm}^2$) with **a** selective corrosion of the ferrite and some attack on austenite, **b** transgranular cracks through an area containing σ -phase and austenite, **c–f** multiple micro-cracks nucleated within austenite

corrosion process, supporting their net cathodic behaviour. Their discrete shape and morphology indicated that these secondary phases are possibly Cr_2N , χ , and/or CrN (Fig. 14c, d).

The same corrosion morphology as with exposure to lower chloride deposition densities was observed under the droplet containing $2856 \mu\text{g}/\text{cm}^2$ chloride (drop 5), showing selective attack on the ferrite with minor attack on the austenite, as can be seen in Fig. 15a, b. The most severe corrosion was observed under this droplet, due to largest deposition density, which in turn affects the corrosion potential. A large number of transgranular stress corrosion micro-cracks were observed in areas containing σ -phase and austenite.

The austenite is susceptible to stress corrosion cracking due to its critical nickel content which was determined to be in the order of 7 % (see Table 1) [78]. The Copson curve shows lowest time to failure, i.e. highest stress corrosion cracking susceptibility for chloride-induced stress corrosion cracking of stainless steels with nickel contents between ~ 7 and ~ 15 % [78]. Stress corrosion micro-cracks were observed in regions containing secondary austenite and σ -phase as shown in Fig. 15b, a region eutectoidically transformed from ferrite. Secondary austenite is depleted in Cr, Mo, and N, and therefore, more prone to corrosion. The nickel content of secondary austenite is somewhat lower

than that of primary austenite [30], and the cracking susceptibility may have been enhanced by the presence of sigma phase. Multiple stress corrosion cracking events were also seen in the primary austenite as shown in Fig. 15c, f, with maximum length of cracks in the aged microstructure of up to 30–35 μm , spanning across several grains. The latter confirms stress corrosion cracking propensity of aged sample when exposed to environment with extremely high chloride concentrations.

Practical relevance

Grade 2205 duplex stainless steel in the as-received condition is typically resistant to localised corrosion and stress corrosion cracking and the material only shows propensity towards corrosion and micro-cracking with exposure to harsh environmental conditions, such as the high chloride concentrations used in Fig. 10. High deposition densities of chloride in high concentrations (close to deliquescence equilibrium of MgCl_2) led to a maximum crack length of 15 μm , which showed minor stress corrosion cracking propensity of the as-received material. Grade 2205 duplex stainless steel has superior stress corrosion cracking resistance to the most common austenitic counterpart alloys 304L and 316L which showed more severe crack developments in similar (or under less aggressive) conditions

[74–76, 79–84]. The 750 °C-aged microstructure, however, was clearly more susceptible to localised corrosion and stress corrosion cracking, which may have implications for welding practice of duplex stainless steels. Grade 2205 duplex stainless steel can be rendered susceptible to AISCC at a temperature of 50 °C, and the calculated threshold temperature (>50 °C) for AISCC in grade 2205 should be re-visited under MgCl₂ exposure conditions [75].

Conclusions

The effect of 750 °C ageing treatment on microstructure development using correlative EBSD and SKPFM techniques has been investigated. The crystallographic phases present were correlated to their local Volta potentials and corrosion behaviours.

1. CrN, Cr₂N, χ -, σ -, and secondary austenite (γ_2) phases precipitated in the microstructure with γ_2 and σ forming the largest secondary phases in size and fraction. The formation of σ , γ_2 , and χ was allotriomorphic, with the σ -phase showing no internal grain boundaries.
2. The σ -phase and γ_2 precipitated within ferrite and at δ/γ interfaces, and χ -phase at δ/γ interfaces only, whilst CrN/Cr₂N was found at δ/γ and σ/γ_2 interfaces and δ/δ boundaries.
3. The as-received microstructure showed 50–70 mV Volta potential differences with δ acting as net anode and γ as net cathode. The Volta potential difference between δ and γ after ageing treatment decreased in certain regions, but Volta potential variations within each phase increased. Local Volta potential extremes were developed indicating enhanced corrosion susceptibility.
4. The σ -phase, Cr₂N, CrN, and inter-granular (IP) χ -phase indicated low electronic activities, i.e. expecting net cathodic behaviour, whilst the intra-granular (IF) χ -phase indicated only enhanced net anodic activity among secondary phases.
5. Selective corrosion of the ferrite was observed in the as-received and the 750 °C-aged condition, with the overall corrosion propensity of secondary phases being in-line with SKPFM observations.
6. Stress corrosion micro-cracks were found in the austenitic phase in the as-received and 750 °C heat-treated conditions after exposure to atmospheric MgCl₂ electrolyte.

Acknowledgements The authors acknowledge Radioactive Waste Management (RWM) (NPO004411A-EPS02) and EPSRC (EP/I036397/1) for financial support. The authors are grateful for the kind provision of Grade 2205 Duplex Stainless Steel plate by Rolled

Alloys. Special thanks also to Dr Christiano Padovani, Radioactive Waste Management Ltd. for valuable discussions.

Open Access This article is distributed under the terms of the Creative Commons Attribution 4.0 International License (<http://creativecommons.org/licenses/by/4.0/>), which permits unrestricted use, distribution, and reproduction in any medium, provided you give appropriate credit to the original author(s) and the source, provide a link to the Creative Commons license, and indicate if changes were made.

References

1. Padovani C (2014) Overview of UK research on the durability of container materials for radioactive wastes. *Corros Eng, Sci Technol* 49:402–409
2. Lo KH et al (2009) Recent developments in stainless steels. *Mater Sci Eng R* 65:39–104
3. Lula et al (1983) Duplex stainless steels. American Society for Metals, Mars
4. Charles J, Bernhardsson S (1991) Duplex stainless steels '91—volume 1. In: Duplex stainless steels '91. Beaune, Les editions de physique
5. Redjaimia A et al (2002) Microstructural and analytical study of heavily faulted Frank-Kasper R-phase precipitates in the ferrite of a duplex stainless steel. *J Mater Sci* 37:4079–4091. doi:10.1023/A:1020023500133
6. Byun S-H et al (2012) Kinetics of Cr/Mo-rich precipitates formation for 25Cr-6.9Ni-3.8Mo-0.3N super duplex stainless steel. *Met Mater Int* 18:201–207
7. Chung HM (1989) Spinodal decomposition of austenite in long-term-aged duplex stainless steel. Argonne National Lab, Lemont
8. Garner FA et al (1986) Ion-induced spinodal-like decomposition of Fe-Ni-Cr invar alloys. *Nucl Instrum Methods Phys Res B* 16:244–250
9. Horvath W et al (1998) Microhardness and microstructure of austenite and ferrite in nitrogen alloyed duplex steels between 20 and 500°C. *Mater Sci Eng A* 256:227–236
10. Padilha AF, Rios PR (2002) Decomposition of austenite in austenitic stainless steels. *ISIJ Int* 42:325–327
11. Liao J (2001) Nitride precipitation in weld HAZs of a duplex stainless steel. *ISIJ Int* 41:460–467
12. Ramirez AJ et al (2004) Secondary austenite and chromium nitride precipitation in simulated heat affected zones of duplex stainless steels. *Sci Technol Weld Join* 9:301–313
13. Sathirachinda N et al (2010) Study of nobility of chromium nitrides in isothermally aged duplex stainless steels by using SKPFM and SEM/EDS. *Corros Sci* 52:179–186
14. Bruch D (2007) Investigations on microstructure, mechanical properties and corrosion resistance of large thickness duplex stainless steel forgings. *Stainless steel world*. KCI Word Publishing, Maastricht
15. Bruch D et al (2008) Mechanical properties and corrosion resistance of duplex stainless steel forgings with large wall thicknesses, *La Metallurgia Italiana*, pp 1–7
16. Nilsson JO (1992) Super duplex stainless steels. *Mater Sci Technol* 8:685–700
17. Örnek C, Engelberg DL (2013) Effect of “475°C embrittlement” on the corrosion behaviour of grade 2205 duplex stainless steel investigated using local probing techniques. *Corrosion management*. The Institute of Corrosion, Northampton, pp 9–11
18. Örnek C et al (2015) Effect of 475°C embrittlement on microstructure development and mechanical properties of grade 2205 duplex stainless steel. *Metall Mater Trans A*

19. Tavares SSM et al (2001) 475°C embrittlement in a duplex stainless steel UNS S31803. *Mater Res* 4:237–240
20. Park C-J, Kwon H-S (2002) Effects of aging at 475°C on corrosion properties of tungsten-containing duplex stainless steels. *Corros Sci* 44:2817–2830
21. Iacoviello F et al (2005) Effect of “475°C embrittlement” on duplex stainless steels localized corrosion resistance. *Corros Sci* 47:909–922
22. Calliari I et al (2009) Measuring secondary phases in duplex stainless steels. *JOM* 61:80–83
23. Cho H-S, Lee K (2013) Effect of cold working and isothermal aging on the precipitation of sigma phase in 2205 duplex stainless steel. *Mater Charact* 75:29–34
24. Elmer JW et al (2007) Direct observations of sigma phase formation in duplex stainless steels using in-situ synchrotron X-ray diffraction. *Metall Mater Trans A* 38:464–475
25. Hsieh C-C, Wu W (2012) Overview of intermetallic sigma (σ) phase precipitation in stainless steels. *ISRN Metall* 16
26. Michalska J, Sozańska M (2006) Qualitative and quantitative analysis of σ and χ phases in 2205 duplex stainless steel. *Mater Charact* 56:355–362
27. Nilsson JO et al (2000) Mechanical properties, microstructural stability and kinetics of σ -phase formation in 29Cr-6Ni-2Mo-0.38N superduplex stainless steel. *Metall Mater Trans A* 31:35–45
28. Nilsson J-O, Chai G (2007) The physical metallurgy of duplex stainless steels. *International Conference & Expo DUPLEX 2007*. Associazione Italiana di Metallurgia, Grado
29. Nilsson J-O, Liu P (1991) Aging at 400–600°C of submerged arc welds of 22Cr-3Mo-8Ni duplex stainless steel and its effect on toughness and microstructure. *Mater Sci Technol* 7:853–862
30. Padilha AF et al (2009) Chi-phase precipitation in a duplex stainless steel. *Mater Charact* 60:1214–1219
31. Pohl M et al (2007) Effect of intermetallic precipitations on the properties of duplex stainless steel. *Mater Charact* 58:65–71
32. Sieurin H, Sandström R (2007) Sigma phase precipitation in duplex stainless steel 2205. *Mater Sci Eng* 444:271–276
33. Cui J et al (2001) Degradation of impact toughness due to formation of R phase in high nitrogen 25Cr-7Ni-Mo duplex stainless steels. *ISIJ Int* 41:192–195
34. Karlsson L et al (1995) Precipitation of intermetallic phases in 22% Cr duplex stainless weld metals—the kinetics of intermetallic phase formation in the temperature range 675°–1000°C (1247°–1832°F) and effects on mechanical properties and corrosion resistance. *Weld J-Incl Weld Res Suppl* 74:28–38
35. Redjaimia A et al (2008) Orientation relationships between the δ -ferrite matrix in a duplex stainless steel and its decomposition products: the austenite and the χ and R Frank-Kasper phases. In: *EMC 2008 14th European microscopy congress 1–5 September 2008, Aachen, Germany*. Springer Berlin Heidelberg, pp. 479–480
36. Pettersson N et al (2015) Precipitation of chromium nitrides in the super duplex stainless steel 2507. *Metall Mater Trans A* 46:1062–1072
37. Ramirez AJ et al (2003) The relationship between chromium nitride and secondary austenite precipitation in duplex stainless steels. *Metall Mater Trans A* 34:1575–1597
38. Charles J, Bernhardsson S (1991) Duplex Stainless Steels ‘91—Volume 2. In: *Duplex Stainless Steels ‘91*. Les editions de physique, Beaune, Bourgogne, France
39. Humphreys FJ (2004) Characterisation of fine-scale microstructures by electron backscatter diffraction (EBSD). *Scripta Mater* 51:771–776
40. Li W et al (2006) Influences of tensile strain and strain rate on the electron work function of metals and alloys. *Scripta Mater* 54:921–924
41. Li W, Li DY (2006) Influence of surface morphology on corrosion and electronic behavior. *Acta Mater* 54:445–452
42. Bockris JOM et al (2002) *Modern electrochemistry 2A*. Fundamentals of electrodiodes, vol 2A. Kluwer Academic Publishers, New York, pp 1–817
43. Sadewasser S, Glatzel T (2012) Kelvin probe force microscopy measuring and compensating microscopy. Springer, Heidelberg
44. Örnek C et al (2015) A corrosion model for 475°C embrittlement in duplex stainless steel—a comprehensive study via scanning Kelvin probe force microscopy. *Corros Sci*
45. Örnek C, Engelberg DL (2015) SKPFM measured Volta potential correlated with strain localisation in microstructure of cold-rolled grade 2205 duplex stainless steel. *Corros Sci* 99:164–171
46. Sathirachinda N et al (2008) Characterization of phases in duplex stainless steel by magnetic force microscopy/scanning Kelvin probe force microscopy. *Electrochim Solid-State Lett* 11:C41–C45
47. Sathirachinda N et al (2009) Depletion effects at phase boundaries in 2205 duplex stainless steel characterized with SKPFM and TEM/EDS. *Corros Sci* 51:1850–1860
48. Sathirachinda N et al (2011) Scanning Kelvin probe force microscopy study of chromium nitrides in 2507 super duplex stainless steel—implications and limitations. *Electrochim Acta* 56:1792–1798
49. Blücher DB et al (2004) Scanning Kelvin probe force microscopy: a useful tool for studying atmospheric corrosion of MgAl alloys in situ. *J Electrochem Soc* 151:B621–B626
50. Rohwerder M, Turcu F (2007) High-resolution Kelvin probe microscopy in corrosion science: scanning Kelvin probe force microscopy (SKPFM) versus classical scanning Kelvin probe (SKP). *Electrochim Acta* 53:290–299
51. Wang R et al (2014) Changes of work function in different deformation stage for 2205 duplex stainless steel by SKPFM. *Procedia Mater Sci* 3:1736–1741
52. Humphreys FJ et al (1999) Electron backscatter diffraction of grain and subgrain structures—resolution considerations. *J Microsc* 195:212–216
53. Frankel GS et al (2001) Characterization of corrosion interfaces by the scanning Kelvin probe force microscopy technique. *J Electrochem Soc* 148:B163–B173
54. Nonnenmacher M et al (1991) Kelvin probe force microscopy. *Appl Phys Lett* 58:2921–2923
55. Marcus P, Mansfeld F (2006) *Analytical methods in corrosion science and engineering*. Taylor & Francis Group, Boca Raton
56. Engelberg DL, Örnek C (2014) Probing propensity of grade 2205 duplex stainless steel towards atmospheric chloride-induced stress corrosion cracking. *Corros Eng Sci Technol* 49:535–539
57. Jackson EMLEM et al (1993) Distinguishing between Chi and Sigma phases in duplex stainless steels using potentiostatic etching. *Mater Charact* 31:185–190
58. Shiao JJ et al (1993) Phase transformations in ferrite phase of a duplex stainless steel aged at 500°C. *Scr Metall Mater* 29:1451–1456
59. Li H et al (2015) Austenite transformation behaviour of 2205 duplex stainless steels under hot tensile test. *Steel Res Int* 86:84–88
60. Liu H, Jin X (2011) Electrochemical corrosion behavior of the laser continuous heat treatment welded joints of 2205 duplex stainless steel. *J Wuhan Univ Technol* 26:1140–1147
61. Bettini E et al (2014) Study of corrosion behavior of a 2507 super duplex stainless steel: influence of quenched-in and isothermal nitrides. *Int J Electrochem Sci* 9:20
62. Kim J-S et al (2012) Mechanism of localized corrosion and phase transformation of tube-to-tube sheet welds of hyper duplex stainless steel in acidified chloride environments. *Jpn Inst Met* 53:9

63. Örnek C, Engelberg DL (2015) Effect of cold deformation mode on stress corrosion cracking susceptibility of 2205 duplex stainless steel, in preparation
64. Örnek C, Engelberg DL (2015) Environment-assisted stress corrosion cracking of grade 2205 duplex stainless steel under low-temperature atmospheric exposure, in preparation
65. Arnold N et al (1997) Chloridinduzierte Korrosion von Nichtrostenden Stählen in Schwimmhallen-Atmosphären Teil 1: elektrolyt Magnesium-Chlorid (30%). *Mater Corros* 48:679–686
66. Aoki S et al (2010) Dissolution behavior of α and γ phases of a duplex stainless steel in a simulated crevice solution. *ECS Trans* 25:17–22
67. Femenia M et al (2001) In situ study of selective dissolution of duplex stainless steel 2205 by electrochemical scanning tunnelling microscopy. *Corros Sci* 43:1939–1951
68. Pettersson RFA, Flyg J (2004) Electrochemical evaluation of pitting and crevice corrosion resistance of stainless steels in NaCl and NaBr. *Outokumpu*, Stockholm, Sweden
69. Deng B et al (2008) Critical pitting and repassivation temperatures for duplex stainless steel in chloride solutions. *Electrochim Acta* 53:5220–5225
70. Aoki S et al (2011) Potential dependence of preferential dissolution behavior of a duplex stainless steel in simulated solution inside crevice. *Zairyo-to-Kankyo* 60:363–367
71. Ebrahimi N et al (2011) Correlation between critical pitting temperature and degree of sensitisation on alloy 2205 duplex stainless steel. *Corros Sci* 53:637–644
72. Örnek C, Engelberg DL (2014) Kelvin probe force microscopy and atmospheric corrosion of cold-rolled grade 2205 duplex stainless steel. *Eurocorr 2014*. European Federation of Corrosion, Pisa, Italy, pp 1–10
73. Lee J-S et al (2014) Corrosion behaviour of ferrite and austenite phases on super duplex stainless steel in a modified green-death solution. *Corros Sci* 89:111–117
74. Prosek T et al (2008) Low temperature stress corrosion cracking of stainless steels in the atmosphere in presence of chloride deposits. *NACE*, vol. Paper No. 08484: NACE International, p 17
75. Prosek T et al (2014) Low-temperature stress corrosion cracking of austenitic and duplex stainless steels under chloride deposits. *Corros Sci* 70:1052–1063
76. Prosek T et al (2009) Low-temperature stress corrosion cracking of stainless steels in the atmosphere in the presence of chloride deposits. *Corros Sci* 65:13
77. Örnek C et al (2012) Effect of microstructure on atmospheric-induced corrosion of heat-treated grade 2205 and 2507 duplex stainless steels. *Eurocorr 2012*. Dechema, Istanbul, Turkey, pp 1–10
78. Cottis B et al (2010) *Shreir's Corrosion*, vol 2. Elsevier B.V., Manchester
79. Cook AB et al (2010) Preliminary evaluation of digital image correlation for in-situ observation of low temperature atmospheric-induced chloride stress corrosion cracking in austenitic stainless steels. *ECS Trans* 25:119–132
80. Cook AB et al (2014) Assessing the risk of under-deposit chloride-induced stress corrosion cracking in austenitic stainless steel nuclear waste containers. *Corros Eng Sci Technol* 49:529–534
81. Lyon SB et al (2010) Atmospheric corrosion of nuclear waste containers. In: *DIAMOND'10 conference decommissioning, immobilisation and management of nuclear waste for disposal*. Manchester, UK
82. Albores-Silva OE et al (2011) Effect of chloride deposition on stress corrosion cracking of 316L stainless steel used for intermediate level radioactive waste containers. *Corros Eng Sci Technol* 46:124–128
83. Padovani C et al (2014) Corrosion control of stainless steels in indoor atmospheres—laboratory measurements under $MgCl_2$ deposits at constant relative humidity (Part 1). *Corrosion* 71:292–304
84. Padovani C et al (2014) Corrosion control of stainless steels in indoor atmospheres—practical experience (Part 2). *Corrosion* 71:246–266